This is a repository copy of *Balancing laminar extension and wave drag for transonic swept wings*.

White Rose Research Online URL for this paper:
https://eprints.whiterose.ac.uk/173267/

Version: Accepted Version

Article:
Zhu, M. and Qin, N. orcid.org/0000-0002-6437-9027 (2021) Balancing laminar extension and wave drag for transonic swept wings. AIAA Journal, 59 (5). pp. 1660-1672. ISSN 0001-1452

https://doi.org/10.2514/1.j059914

© 2021 by the authors. Published by the American Institute of Aeronautics and Astronautics, Inc., with permission. This is an author-produced version of a paper subsequently published in AIAA Journal. Uploaded in accordance with the publisher's self-archiving policy.

Reuse
Items deposited in White Rose Research Online are protected by copyright, with all rights reserved unless indicated otherwise. They may be downloaded and/or printed for private study, or other acts as permitted by national copyright laws. The publisher or other rights holders may allow further reproduction and re-use of the full text version. This is indicated by the licence information on the White Rose Research Online record for the item.

Takedown
If you consider content in White Rose Research Online to be in breach of UK law, please notify us by emailing eprints@whiterose.ac.uk including the URL of the record and the reason for the withdrawal request.

eprints@whiterose.ac.uk
https://eprints.whiterose.ac.uk/

Balancing Laminar Extension and Wave Drag by Unlocking Wing Sweep and Shock-Control

Maolin Zhu[1]
Nanjing University of Aeronautics and Astronautics, Nanjing, People's Republic of China

Ning Qin[2]
University of Sheffield, Sheffield, England S1 3JD, United Kingdom

At transonic condition, the design of natural laminar flow (NLF) wing is challenging, as the extension of the laminar flow needs to be finely balanced with the potential wave drag increase. To achieve this balance, it is proposed to unlock the wing sweep and introduce three-dimensional (3-D) contour shock-control bump (SCB) in the optimization of NLF infinite swept wing aiming at total drag reduction. A 3-D Reynolds-Averaged Navier-Stokes flow solver is extended to incorporate laminar-turbulent transition prediction due to streamwise and crossflow instabilities. The flow solver is integrated in a gradient-based optimization framework. The transition criteria including streamwise and crossflow instabilities are coupled in the sensitivity calculation using a discrete adjoint solver. Transonic design optimization of the sectional profile and wing sweep angle is first conducted at a Mach number of 0.78. The optimization managed to alleviate the shock wave, reducing the pressure drag while it failed to extend the laminar flow. Further, a combined optimization of the wing with a parameterized SCB at the same condition is carried out. The optimized wing with SCB features a long favorable pressure gradient region and a low sweep angle which allows for a large proportion of laminar flow without significant pressure drag. The shock wave is controlled by the 3-D bump and the SCB has little effect on the upstream flow.

[1] Ph.D. Research Student, College of Aerospace Engineering; zmlnuaa@gmail.com

[2] Professor of Aerodynamics, Department of Mechanical Engineering; n.qin@sheffield.ac.uk. Associate Fellow AIAA (Corresponding Author).

Nomenclature

$B_{k,N}$ = Bernstein polynomials

c = chord length

C_d = drag coefficient

C_{df} = skin friction drag coefficient

C_{dp} = pressure drag coefficient

C_f = skin friction coefficient

C_l = lift coefficient

C_p = pressure coefficient

F = objective function

H_{cf} = crossflow shape factor

H_k = streamwise shape factor

M = Mach number

n_{CF} = crossflow amplification factor

n_{TS} = streamwise amplification factor

N = composite amplification factor

NDV = number of design variables

p = pressure

$\boldsymbol{P}$ = vector of primitive flow variables

$\boldsymbol{Q}$ = vector of conservative flow variables

r = leading edge radius

$\bar{R}$ = attachment-line similarity parameter

Re_{cf} = crossflow Reynolds number

Re_θ = momentum thickness Reynolds number

$\boldsymbol{R}$ = vector of flow residuals

$\boldsymbol{R}_{tr}$ = vector of transition residuals

T = temperature

U = velocity magnitude

V = wing volume

w = crossflow velocity component

x, y, z = Cartesian coordinates in streamwise, vertical and spanwise directions, respectively

$\boldsymbol{X}_f$ = vector of forced transition location

$\boldsymbol{X}_p$ = vector of predicted transition location

$\boldsymbol{\beta}$ = vector of design variables

γ = ratio of specific heat

δ = boundary layer thickness

δ_{cf} = crossflow thickness

$\boldsymbol{\lambda}$ = adjoint vector

$\boldsymbol{\lambda}_{tr}$ = transition adjoint vector

Λ = sweep angle

ν = kinematic viscosity

ρ = density

$\boldsymbol{\chi}$ = vector of volume grid

Subscripts

cr = critical value

e = at boundary layer edge

w = at wall surface

∞ = at farfield

I. Introduction

The aerodynamic performance of civil transport aircraft has been greatly improved over the past decades. To the present day, every drag count reduction is becoming hugely challenging for the current aerodynamic configuration. The Europe's vision for future air transport, Fight Path 2050 [1], sets a target for a 75% reduction of CO_2 emissions from the 2000 reference. More challenging general targets have been set by various countries in the world more recently, e.g. the Green Deal, Carbon Neutral and

Net-Zero-Emission by 2050s. For modern transport aircraft, extending the portion of laminar flow on the wing surface is one of the approaches to reduce skin friction drag that offers a large potential economic savings and improvements in environmental protection. Some pioneering practical applications of natural laminar flow (NLF) can be found on the nacelles on Boeing 787 [2], the winglet on the 737 [2] and the wing on the supersonic Honda business jet [3]. Despite of the limited practical applications of NLF, the design for natural laminar flow wings is still a huge challenge at the Mach number of the current regional transport aircraft.

Considering airfoil boundary layer transition, Khayatzadeh and Nadarajah [4] performed two-dimensional (2-D) NLF airfoil optimizations at subsonic and low-Reynolds-number conditions. The adjoint equations of the γ-$Re_{\theta t}$ transition model were derived and implemented in the design framework for gradient evaluations in their research. Driver and Zingg [5] coupled the discrete-adjoint and finite-difference gradient calculations to incorporate the effect of the laminar-turbulent transition in the optimization. More recently, Rashad and Zingg [6] considered some more realistic flight conditions for NLF airfoil designs. Large proportion of laminar flow on the airfoil surface has been achieved but, the problem for NLF design at higher transonic speeds involving shock waves is still a challenging issue.

In the transonic regime, the required favorable streamwise pressure gradient for NLF airfoil design generally results in a stronger shock wave on the suction surface. A balance between the conflicting requirements for lower skin friction drag and wave drag is difficult to strike. Amoignon *et al.* [7] conducted some preliminary work in transonic NLF airfoil optimization design using a gradient-based optimization method. A composite objective function was considered to delay the laminar-turbulent transition by minimizing the disturbance kinetic energy and reduce simultaneously

the pressure drag. The gradients of objective function with respect to the design variables were computed based on the solutions of the adjoints of the Euler equations, the laminar boundary layer equations and the parabolized stability equations. Gao *et al.* [8] achieved NLF on a supercritical airfoil to improve its aerodynamic characteristics. The γ-$Re_{\theta t}$ transition model combined with the shear stress transport k-ω turbulence model was adopted to predict boundary layer transition. The non-dominated sorting genetic algorithm-II was used as the searching algorithm, and a surrogate model based on the Kriging models was employed to improve the efficiency of the optimization system.

For three-dimensional (3-D) transonic NLF wing design, in addition to the streamwise (Tollmien-Schlichting, T-S) instability, the wing sweep needs to be controlled to avoid leading-edge attachment-line (A-L) transition [9] and crossflow (C-F) instability induced transition [10]. The experience of the ELFIN flying tests [10] shows that at wing sweep over 20°, the boundary layer is prone to crossflow instability. On the other hand, a lower sweep angle leads to a higher effective Mach number normal to the wing leading edge which offsets the benefit of NLF with increased wave drag, or even worse, results in shock induced separation and drag divergence [11,12]. It is noted that in the previous studies reviewed, the design Mach number for 3-D transonic NLF wing is normally set to be lower than the cruising speed of a modern regional transport aircraft (typically $M \geq 0.78$), as shown in the following literature. Zhang *et al.* [13] and Han *et al.* [14] conducted a thorough study in 3-D transonic NLF wing optimization design for the regional transport aircraft. The optimizations were performed at Mach numbers of 0.76 and 0.75, respectively. Lee and Jameson [15] conducted a gradient-based NLF wing design at a Mach number of 0.74 and the transition criteria were not included in their gradient evaluations and their research focused on the reduction of the wave drag. In a European Laminar Aircraft Demonstrator project [16, 17], NLF technology has been investigated on a

low sweep outer wing section on the large transport aircraft Airbus A340 in flight tests, in which the cruising Mach number was not published. Streit *et al.* [18] and Seitz *et al.* [12] investigated the feasibility of forward swept laminar wing design for the typical transport aircraft, A320-200, with a design Mach number is 0.78.

The realization of transonic natural laminar flow at higher transonic Mach number is still challenging and demanding. In order to tackle the stronger shock wave resulting from the favorable streamwise pressure gradient for NLF pressure distribution and lower wing sweep from current dominant high sweep design, shock-control is crucial. Shock-control research for transonic wings dates back to the 1940s, where suction was considered to avoid shock induced separation in a transonic wind tunnel [19]. In 1992, Ashill *et al.* [20] first proposed 2-D shock-control bump (SCB) to reduce wave drag on laminar flow airfoils. The European research project EUROSHOCK II [21] conducted a thorough study of different shock-control methods and SCB was found to be the most effective shock-control device [22]. In 2000, Birkemeyer *et al.* [23] investigated the shock-control device of 2-D contour bumps experimentally and numerically on a transonic swept wing. They found that the influence of sweep on the bump effectiveness was rather small, and the drag reduction is slightly lower for the swept wing than the 2-D airfoil (i.e., zero sweep) case. Qin *et al.* [11,24,25] proposed and optimized 3-D contour bumps for NLF transonic airfoils and wings. Their numerical studies show that optimized 3-D bumps could effectively reduce the wave drag in a wider operational range. The experimental and computational studies by Zhu *et al.* [26] demonstrated the effectiveness of SCBs for a low-sweep NLF wing. König *et al.* [22] conducted experimental and numerical studies to evaluate the drag reduction of an array of discrete three-dimensional shock control bumps mounted on an un-swept supercritical wing. Approximately 10% drag reduction was achieved in the drag-rise region in their

experiment. Some fundamental understanding of the flow physics for shock control bumps can be found in Barbinsky *et al.* [27] for different ramp bumps mounted on the floor of a supersonic wind tunnel. In order to extend the laminar flow region and meanwhile alleviate the shock wave, Tang *et al.* [28] developed a distributed Nash Evolutionary Algorithms for the transonic optimization design of NLF airfoil with SCB. Two objectives were used in their optimization: optimizing the airfoil shape to delay transition, and the location and shape of a shock-control bump to reduce wave drag. However, the optimization does not aim for the minimum total drag and therefore the balance of the two factor has not been investigated in relation to the total drag reduction. Bruce and Colliss [29] gave a detailed review of studies on shock-control bumps.

This paper reports an aerodynamic wing shape optimization aiming for a balance of the two factors, transition and shock wave, for total drag reduction at high transonic Mach number by combining natural laminar flow profiling with shock-control bump. To achieve this, a free-transition flow solver capable of predicting laminar-turbulent transition including streamwise and crossflow instabilities is first described in Section II. A discrete adjoint solver incorporating the transition criteria is presented. The parameterizations of the infinite swept wing and 3-D SCBs are described in Section III. The capability of the flow solver in transition prediction is then validated by available experimental data. Section V presents the transonic aerodynamic shape optimization results for an infinite swept wing with or without SCB. The effectiveness of the combined optimization is demonstrated in comparison with the baseline and optimization without SCB. Some conclusions are drawn in Section VI.

II. Numerical Methods

A. 3-D Wing Transition Criteria

For a swept wing, three transition mechanisms are present: streamwise, crossflow and attachment-line transitions. The simplified e^N envelope method for transition prediction due to T-S and C-F instabilities is adopted in this study. Following the work of Drela and Giles [30], the T-S amplification factor can be calculated along the streamwise direction s by

$$n_{TS} = \int_{s_0}^{s} \frac{dn_{TS}}{ds} ds = \int_{s_0}^{s} \frac{m+1}{2} \cdot l \cdot \frac{1}{\theta} \cdot \frac{dn_{TS}}{d\,\mathrm{Re}_\theta} ds \,. \tag{1}$$

The functions in the equation are given as

$$\frac{dn_{TS}}{d\,\mathrm{Re}_\theta} = 0.01\sqrt{\left[2.4H_k - 3.7 + 2.5\tanh\left(1.5H_k - 4.65\right)\right]^2 + 0.25}\,, \tag{2}$$

$$m = \left(0.058\frac{\left(H_k - 4\right)^2}{H_k - 1} - 0.068\right) \cdot \frac{1}{l}\,, \tag{3}$$

$$l = \frac{6.54H_k - 14.07}{H_k^2}\,. \tag{4}$$

For crossflow amplification factor, the formula developed by Sturdza [31] is used in this work. The crossflow n-factor is calculated by

$$\frac{dn_{CF}}{ds} = \frac{2.128}{\delta_{cf}}\left(\frac{w_{\max}}{U_e}\right)^{1.07} H_{cf}\left(\frac{T_e}{T_w}\right)^{0.4}\left(1 + \left|H_{cf} - 0.35\right|^{1.5}\right)\left[\tanh\left(\frac{\mathrm{Re}_{cf} - \mathrm{Re}_{cf\,0}}{336 - \mathrm{Re}_{cf\,0}}\right)\right]^{0.4}\,, \tag{5}$$

$$n_{CF} = \int_{s_0}^{s} \frac{dn_{CF}}{ds} ds\,. \tag{6}$$

The critical crossflow Reynolds number, Re_{cf0}, is related to the shape factor of crossflow velocity profile. The relationship between critical Reynolds number and crossflow shape factor typically at transonic condition in Ref.[32] is adopted.

The composite amplification factor [31]

$$N = \sqrt{\left(n_{TS} / n_{TS,cr}\right)^2 + \left(n_{CF} / n_{CF,cr}\right)^2} \tag{7}$$

is used to take into account the interference between streamwise and crossflow instabilities. Laminar-turbulent transition occurs when N reaches unity. The critical amplification factors, $n_{TS,cr}$ and $n_{CF,cr}$, are dependent on the test conditions, such as noise, freestream turbulence intensity and surface roughness and they are user specified based on experimental correlations for given applications [6].

In addition to T-S and C-F instabilities, attachment-line transition is another mechanism for transition for swept wing. Poll [33] proposed the local attachment-line Reynolds number

$$\bar{R} = \sqrt{U_\infty r \sin(\Lambda)\tan(\Lambda)/(2\nu_\infty)} \tag{8}$$

based on the leading edge radius r, the sweep angle Λ and the freestream properties, as the A-L transition criterion. A critical value of 245 was suggested by Poll [33]. During the optimization, the attachment-line transition criterion is regarded as a constraint to avoid a fully turbulent wing.

B. Coupling of the RANS Solver and Transition Prediction Method

The transition prediction method is incorporated into an in-house 3-D RANS solver [34,35]. The algebraic turbulence model of Baldwin-Lomax [36] is employed for turbulent boundary layers. This simple model is chosen for its numerical and algorithmic efficiency for optimization, and its reasonable accuracy for attached turbulent boundary layers. The free-transition prediction is achieved through an iterative process which has been employed by several researchers [6,37,38]. The implementation for the iterative procedure of the free-transition flow solver works as follows:

1) The RANS solver is started with initial forced transition points $\boldsymbol{X}_f$ on each spanwise section, given as

$$\mathbf{X}_f = \left(x_{f,upper,1}, x_{f,lower,1}, x_{f,upper,2}, x_{f,lower,2}, ..., x_{f,upper,n}, x_{f,lower,n}\right), \tag{9}$$

where n is the number of sections. Once the total residual $\boldsymbol{R}$ drops to a given tolerance the RANS solver is stopped. The transition prediction module is then invoked.

2) Using the compressible Bernoulli equation [39], the velocity at the boundary edge is calculated from the wall pressure by

$$U_e = \sqrt{U_\infty{}^2 - \frac{2\gamma}{\gamma-1}\frac{p_\infty}{\rho_\infty}\left[\left(\frac{p_w}{p_\infty}\right)^{\frac{\gamma-1}{\gamma}} - 1\right]}. \tag{10}$$

The boundary layer thickness δ is found in the off-wall direction for the point U=0.99U_e. The laminar boundary layer parameters are then directly obtained from RANS solution. Downstream the transition location, the parameters are extrapolated from the laminar boundary layer using a linear extrapolation [37]. It has been shown that under a sufficient mesh resolution, the laminar boundary layer parameters extracted from the RANS solution can be used for transition prediction [6,39]. The grid refinement studies will be presented in Section IV. At each spanwise section, the T-S and C-F amplification factors on the upper and lower surfaces are calculated. The predicted transition points in each spanwise section form a new vector, $\boldsymbol{X}_p$ defined as

$$\mathbf{X}_p = \left(x_{p,upper,1}, x_{p,lower,1}, x_{p,upper,2}, x_{p,lower,2}, ..., x_{p,upper,n}, x_{p,lower,n}\right). \tag{11}$$

3) Transition residual $\boldsymbol{R}_{tr}$ is defined by

$$\mathbf{R}_{tr} = \mathbf{X}_f - \mathbf{X}_p. \tag{12}$$

If the L_2-norm of $\boldsymbol{R}_{tr}$ drops to a given tolerance, the free-transition flow solver is judged to be converged. If not, a new forced transition point vector based on the predicted and the former forced transition points is updated by

$$\mathbf{X}_f^{new} = \mathbf{X}_f^{old} - \sigma\left(\mathbf{X}_f^{old} - \mathbf{X}_p\right). \tag{13}$$

The under-relaxation factor σ is set to 0.8 for a good compromise between efficiency and robustness. The RANS solver is called again with the updated forced transition points until the

transition residual is converged.

C. Discrete Adjoint Solver Coupled with Transition Criteria

In this research, the transition criteria including the streamwise and crossflow instabilities are incorporated into the sensitivity calculations of the objective function to the design variables. The objective function, total drag is written as

$$F = F\left(\overline{\mathbf{P}}\left(\mathbf{P}(\boldsymbol{\beta}), \mathbf{X}_f(\boldsymbol{\beta})\right), \boldsymbol{\chi}(\boldsymbol{\beta}), \boldsymbol{\beta}\right). \tag{14}$$

The detailed differentiation of the equation can be found in LeMoigne and Qin [34] for the discrete adjoint RANS solver without transition models. Following the approach proposed by Rashad and Zingg [6] to incorporate the transition model, the transition adjoint vector $\boldsymbol{\lambda}_{tr}$ is introduced and the adjoint equation systems are given as

$$\begin{cases} \left(\dfrac{\partial F}{\partial \mathbf{P}}\right)^t + \boldsymbol{\lambda}^t \dfrac{\partial \mathbf{R}}{\partial \mathbf{P}} + \boldsymbol{\lambda}_{tr}^t \dfrac{\partial \mathbf{R}_{tr}}{\partial \mathbf{P}} = 0 & \text{(a)} \\ \left(\dfrac{\partial F}{\partial \mathbf{X}_f}\right)^t + \boldsymbol{\lambda}^t \dfrac{\partial \mathbf{R}}{\partial \mathbf{X}_f} + \boldsymbol{\lambda}_{tr}^t \dfrac{\partial \mathbf{R}_{tr}}{\partial \mathbf{X}_f} = 0 & \text{(b)} \end{cases}. \tag{15}$$

The equation system is solved using the incremental iteration method [34]

$$\left[\frac{1}{\Delta t}\frac{\partial \mathbf{Q}}{\partial \mathbf{P}} + \frac{\partial \tilde{\mathbf{R}}(\mathbf{Q})}{\partial \mathbf{P}}\right]^t {}^n\Delta\lambda = -\left\{\left[\frac{\partial F}{\partial \mathbf{P}} + \left(\frac{\partial \mathbf{R}_{tr}}{\partial \mathbf{P}}\right)^t \boldsymbol{\lambda}_{tr}^n\right] + \left(\frac{\partial \mathbf{R}(\mathbf{Q})}{\partial \mathbf{P}}\right)^t \boldsymbol{\lambda}^n\right\}, \tag{16}$$

with

$$\begin{cases} \boldsymbol{\lambda}^{n+1} = \boldsymbol{\lambda}^n + {}^n\Delta\boldsymbol{\lambda} \\ \boldsymbol{\lambda}_{tr}^{n+1} = -\left(\dfrac{\partial \mathbf{R}}{\partial \mathbf{X}_f}\right)^t \boldsymbol{\lambda}^{n+1} \end{cases}. \tag{17}$$

It is noted that in Rashad and Zingg's implementation for airfoil optimization [6], $\boldsymbol{\lambda}_{tr}$ is determined by T-S instability only. In the present formulation for 3-D wings, both the T-S, Eq.(1), and C-F, Eq.(6) instabilities are included. This is directly reflected in the calculation of $\dfrac{\partial \mathbf{R}_{tr}}{\partial \mathbf{P}}$ in Eq.(16) which are stored before the iterative solution of the adjoint system. The sensitivities of the objective function to

the design variables are then simplified to

$$\frac{dF}{d\beta_k} = \left(\frac{\partial F}{\partial \boldsymbol{\chi}}\right)^t \frac{d\boldsymbol{\chi}}{d\beta_k} + \boldsymbol{\lambda}^t \frac{\partial \mathbf{R}}{\partial \boldsymbol{\chi}} \frac{d\boldsymbol{\chi}}{d\beta_k} + \boldsymbol{\lambda}_{tr}^t \frac{\partial \mathbf{R}_{tr}}{\partial \boldsymbol{\chi}} \frac{d\boldsymbol{\chi}}{d\beta_k} \,. \tag{18}$$

The terms $\frac{\partial \mathbf{R}_{tr}}{\partial \boldsymbol{\chi}} \frac{d\boldsymbol{\chi}}{d\beta_k}$ are calculated using the finite-difference method and the other terms except the adjoint vectors in the equation are calculated by application of the chain rule of differentiation to the flow solver routines that compute the residual and the objective function.

III. Wing surface and Shock-Control Bump Parameterizations

A. Bézier-Bernstein Parameterization of the Wing Profile

A Bézier-Bernstein parameterization is employed to represent the airfoil section modification during the optimization process. A perturbation in *y*-direction is added to the original shape, thus

$$y_{current} = y_{initial} + \delta y \,, \tag{19}$$

where

$$\delta y = \sum_{k=0}^{N} B_{k,N}\left(\bar{u}\right)\beta_k \,, \tag{20}$$

with the Bernstein polynomials

$$B_{k,N}\left(\bar{u}\right) = \left\{N!/\left[k!(N-k)!\right]\right\}\bar{u}^k\left(1-\bar{u}\right)^{N-k} \,. \tag{21}$$

The normalized arc length $\bar{u}$ is taken as

$$\bar{u} = \sqrt{x} \,, \tag{22}$$

where x is the non-dimensionalized streamwise position of the point of ordinate $y_{initial}$.

This parameterization is applied independently to the upper and lower surface curves of the airfoil section with 10 design variables on each curve. The leading and trailing edge points are fixed. One additional design variable controls the change in angle of incidence of the whole section. This

parameterization is applied to the infinite swept wing's streamwise sectional profile. It is important to include the wing sweep angle as a design variable to allow its coupling with the profile design variables in the optimization, as have been done before by Le Moigne and Qin [40].

B. Shock-Control Bump Parameterization

Figure 1 shows the parameterization of a 3-D smooth contour bump according to Qin *et al.* [25]. Six key parameters that affect the bump performance based on the previous studies are chosen. These are the bump length, bump crest position along the streamwise direction, relative position of the bump crest to bump length, bump height, total span and relative span. The total span determines the number of 3-D bumps per unit wing span and the relative span controls the effective bump width and the spanwise spacing between the neighboring bumps. The shape of the x-y plane at the middle section of the bump is represented by a cubic spline expression. The same expression is used to model the variation of the y-z plane shape across various streamwise locations of the bump, which then defines the full geometrical shape of the 3-D bump. The gradient at the bump crest is set to zero and the intersections at the base of the bump are treated such that the continuity of the gradient at the intersection point with the wing surface is maintained.

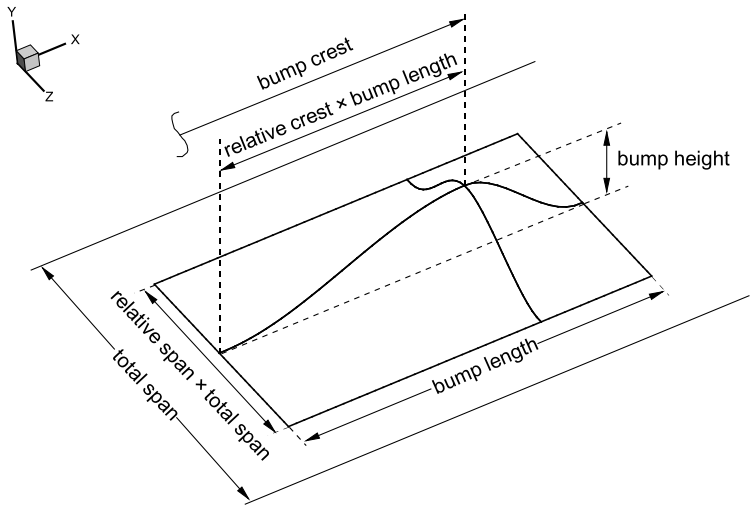

Fig.1 3-D contour SCB's geometry and parameterization.

Figure 2 shows the top view of an infinite swept wing with a 3-D bump on the upper surface. The bump region is bound by the solid red lines. It can be seen that the bump's longitudinal axis (dashed red line) is parallel to the freestream direction. The bump shape is also swept due to the sweep angle, as shown in Figure 2. Once the wing surface with shock-control bump is modified, the computational grid around the whole geometry has to be updated. This is carried out through an algebraic grid deformation technique that propagates smoothly the geometry change through the volume grid.

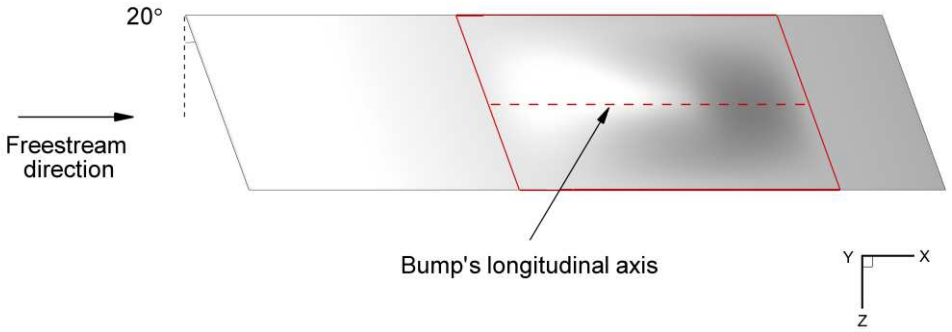

Fig.2 Top view of an infinite swept wing with a 3-D bump (red solid lines).

IV. Verification and Validation

A. NLF0416

The test case of NLF0416 airfoil was used to validate the current solver's capability of transition prediction due to T-S instability. As the boundary layer parameters are directly extracted from RANS solution, a high grid quality is required for transition prediction. Tables 1 and 2 give the results of grid refinement and convergence studies for verification of the numerical solution. The calculation was performed at M=0.2, Re_c=4×10^6 and α=2.0°. The critical N-factor was taken to be 9.0. By comparing the first three rows in Table 1, a streamwise nodal distribution of 377 nodes of the C-type grid was

found to be adequate. For the wall-normal grid refinement that considers 377×74, 377×143 and 377×200 nodes, changing the resolution off the wall from 143 to 200 has a small effect on the drag coefficient, but slows down the convergence of the computation. Therefore, 143 nodes in the off-wall direction was adopted considering computational efficiency, especially for 3D cases. Finally, a C-type grid of 377×143 nodes was used with 300 nodes on the airfoil surfaces. In the boundary layer, there were about 30 nodes around the leading edge and about 90 nodes near the trailing edge in the wall normal direction. The farfield boundary is 40 chord length away from the airfoil in all directions. The height of the first grid is $5.0\times10^{-6}\,c$ and the values of $y+$ on the airfoil surfaces are all less than 1.0 from the solutions. Table 2 demonstrates that when the L_2-norm of the flow residual is reduced to 10^{-6}, the flowfield is basically converged.

Table 1 Grid refinement study of NLF0416 at M=0.2, Re_c=4×10^6 and α=2.0°.

	237×143	377×143	517×143	377×74	377×200
C_l	0.759	0.759	0.759	0.758	0.760
C_d	0.00697	0.00688	0.00690	0.00746	0.00680

Table 2 Convergence study of NLF0416 at M=0.2, Re_c=4×10^6 and α=2.0°.

	10^{-4}	10^{-6}	10^{-8}
C_l	0.762	0.759	0.759
C_d	0.00714	0.00688	0.00687

Figure 3 gives the calculated transition locations at M=0.2, Re_c=4×10^6 for a range of lift conditions and the transition band was provided in the experiment conducted by Somers [41]. The predicted transition locations on the wing's upper and lower surfaces both fall within the region of the experimental values. Figure 4 compares the drag polar of experimental and computational data. As

seen in Figure 4, the predicted drag coefficients in free-transition flow compare well with the experimental data.

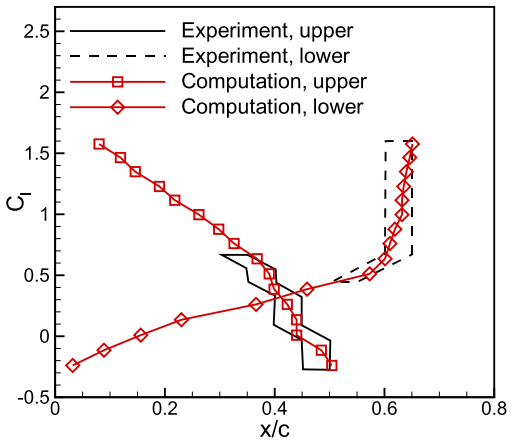

Fig.3 Comparison of transition location on the upper and lower surfaces of NLF0416.

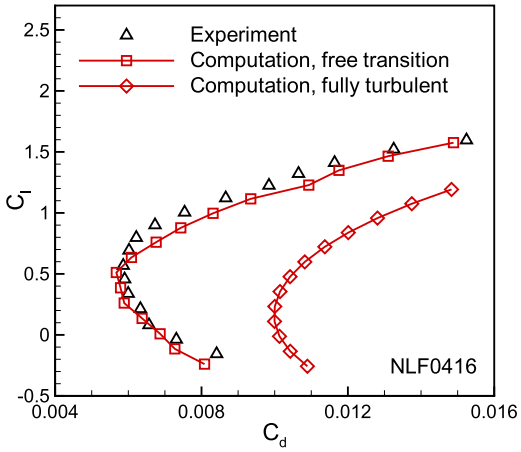

Fig.4 Drag polar comparison of NLF0416.

B. NACA 64_2A015

Next, the 3-D transition prediction capability is investigated. Figure 5 presents a comparison between the predicted transition location and the experimental data of an infinite swept wing with the NACA 64_2A015 sectional profile obtained by Boltz *et al.* [42]. Note here both T-S and C-F instabilities are incorporated in the transition model. Periodic boundary condition is applied at both ends of the model for the infinite swept wing. A C-type mesh with 377×143 nodes was adopted after a grid

sensitivity study. Three nodes are distributed in the spanwise direction for the implementation of the periodic boundary. According to Refs. [38,43], the critical amplification factors for T-S and C-F instabilities were calibrated using the experimental data [42] and were set to 9.0 and 11.0 respectively in this paper. At a range of conditions for Reynolds number Re=4×10^6 to 7.55×10^6, angle of attack α = -3° to -1° and sweep angle Λ = 20° to 50°, the transition locations on the upper surface in the computational and experimental results compare reasonably well, as shown in Figure 5. In Figure 5(a), T-S instability dominates transition at Reynolds number of 4×10^6. As the Reynolds number increases, transition location moves forward and C-F instability prevails when the Reynolds number is greater than 5×10^6. Figure 5(b) shows the transition location in a range of angles of attack. Transition is determined by C-F instability from α = -3° to -1.5°. The results at different sweep angles are shown in Figure 5(c). It shows that C-F instability dominates at Λ = 40° and 50°.

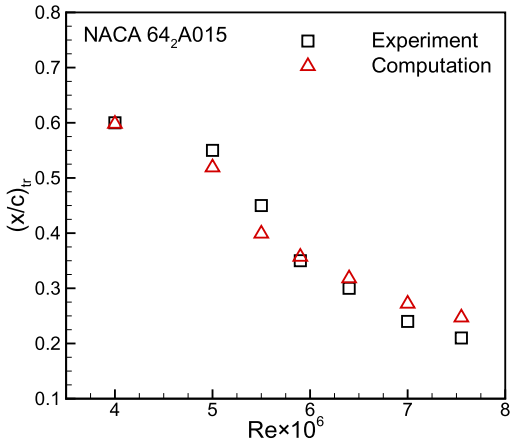

a) Transition location v.s. Reynolds number at M=0.27, Λ=50°, α=-1.0°

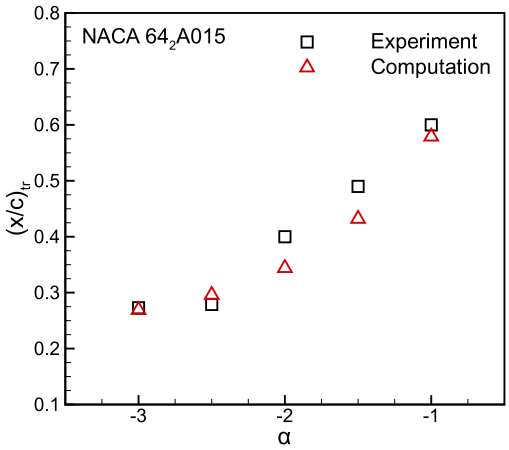

b) Transition location v.s. Angle of attack at M=0.27, Re=5.0×10^6, Λ=40°

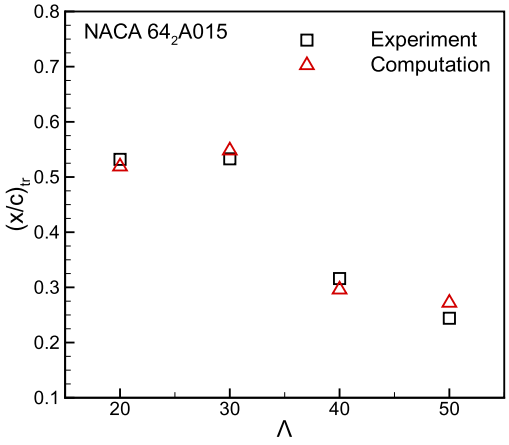

c) Transition location v.s. Sweep angle at M=0.27, Re=7.0×10^6, α=-1.0°

Fig.5 Comparison of upper surface transition location of NACA 64$_2$A015 at different conditions.

V. Results and Discussions

The optimization problems in this paper are a constrained total drag minimization for an infinite swept wing with or without shock-control bump. The 377×143 mesh is adopted in the streamwise and wall normal directions of the wing, shown in Fig. 6, resulting from the grid refinement studies. Periodic boundary condition was applied for the side planes, as shown in Figure 6. A gradient-based sequential quadratic programming optimizer is adopted for searching the optimum design based on the calculated

objective function, the constraints and the sensitivity gradients from the adjoint solver. The optimizations were carried out at a minimum lift coefficient C_l^* and constraints on the wing volume V and attachment-line Reynolds number in Eq.(8). The volume has a lower bound of V_0 and an upper bound of $2V_0$ while V_0 corresponds to the value of the baseline wing. The volume is constrained in the section parallel to the freestream direction. The upper and lower surfaces are free to deform within a certain range. It should be noted that Mach number and aerodynamic coefficients (C_p, C_l *etc*.) are non-dimensionalized using the flow quantities at farfield throughout this paper. The critical amplification factors for T-S and C-F instabilities are specified at 9.0 and 11.0 respectively in the optimization. The optimization model is defined as follows:

$$\text{Minimize} \quad C_d$$

$$\text{Subject to} \quad C_l \geq C_l^*$$

$$V_0 \leq V \leq 2V_0$$

$$\beta_k^l \leq \beta_k \leq \beta_k^u \text{ , } k=1, NDV$$

$$\overline{R} \leq 245$$

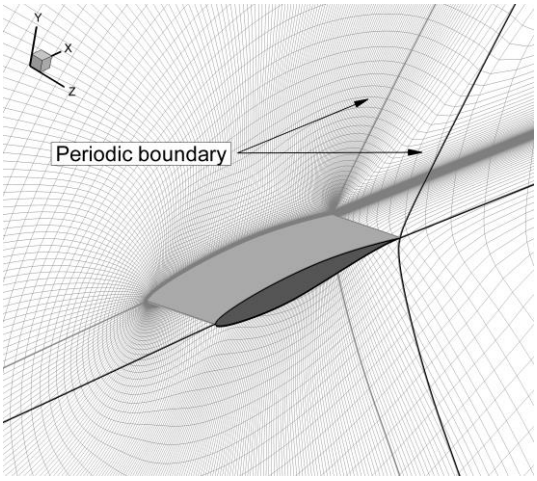

Fig.6 Computational domain around the infinite swept wing.

A. Optimization of an Infinite Swept Wing

The optimization has 18 parameters consisting of 16 Bézier parameters for the wing section profile, the angle of attack and the sweep angle. The initial geometry is an infinite swept wing with RAE2822 section in the streamwise direction. The initial sweep angle is set to 20° which is regarded as a critical value, beyond which the C-F instability becomes important as pointed out by Schrauf [10]. The wingspan is set to a quarter of the chord length in the computation, as shown in Figure 6.

The optimization was conducted at the cruising conditions of a typical regional jet, e.g. Bombardier CRJ-900[44], which cruises at a Mach number of 0.78 with a service ceiling of 41000 ft. The design Mach number in this paper is 0.78. The minimum lift coefficient C_l^* is approximated as 0.5 and the Reynolds number based on chord is 15×10^6. The constraints are satisfied during the optimization, including the lift, volume and attachment-line transition. The drag optimization results in a substantial increase of the sweep angle to 28.6° due to the strong transonic shock at the original lower sweep. The sectional profiles in the streamwise direction of the baseline and optimized wings are compared in Fig.7. The main visible difference in the profiles is on the upper surface between $0.2c$ and $0.8c$. It is understandable that this change is subtle due to the high sensitivity of the objective (drag) to small changes in the profile design variables in transonic flow.

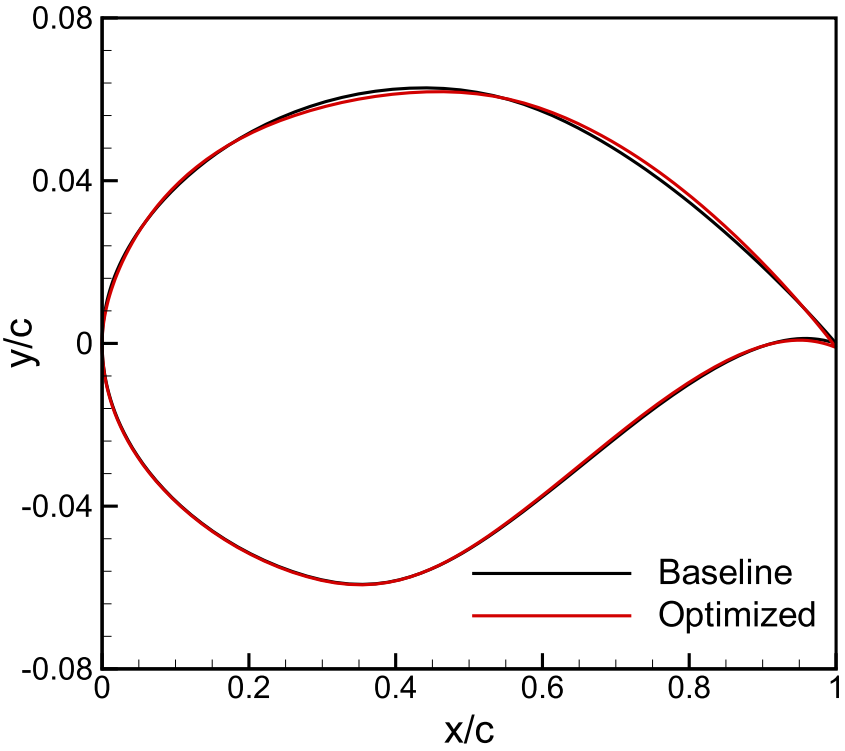

Fig.7 Comparison of the sectional profiles.

Figure 8 gives the pressure coefficient contours on the periodic boundary and wing upper surface. For the infinite swept wings, the flow variation in the spanwise direction is zero as confirmed in the surface contour. It can be seen that the optimized wing leads to a higher sweep angle to alleviate the strong shock wave on the upper surface of the baseline wing, as shown in Figures 8(a) and 8(b). The streamwise pressure distributions in Figure 9 show that the shock wave on the optimized wing moves upstream from around x/c=0.6 to x/c=0.2 and is weakened. Transition locations are given on the pressure distributions using solid squares with corresponding colors.

Figure 10 compares the streamwise skin friction coefficients for the baseline and optimized wing. No flow separation is observed in both cases. It can be seen that transition location on the upper surface moves very slightly, triggered by the weak shock around x/c=0.2, as shown in Figure 9. On the lower surface, transition moves upstream as the sweep angle increases, although favorable pressure gradient is maintained. The reason for this is presented in the following discussion.

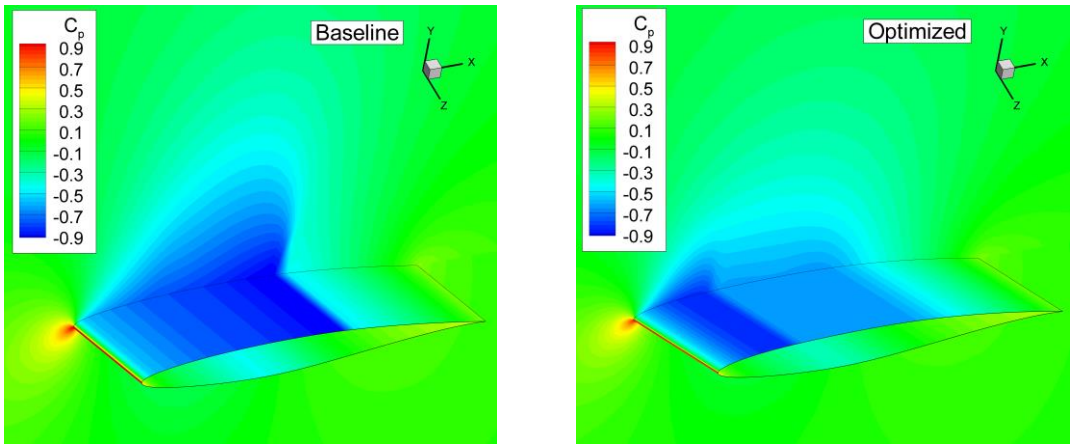

a) Baseline wing **b) Optimized wing**

Fig.8 Pressure coefficient contours on the periodic boundary and wing's upper surface.

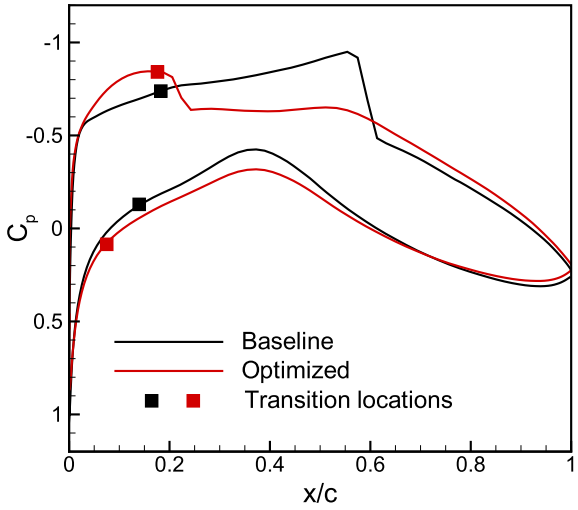

Fig.9 Comparison of the pressure coefficient distributions.

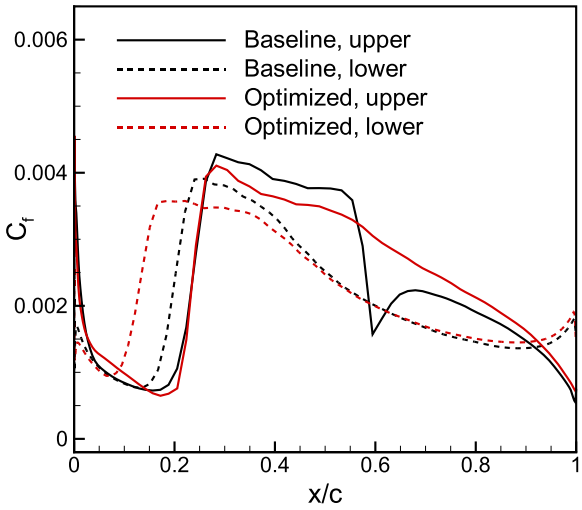

Fig.10 Comparison of the skin friction coefficient distributions on the wing's upper and lower surfaces.

In addition to the attachment-line transition, laminar-turbulent transition in three-dimensional boundary layer is determined by the interaction between T-S and C-F instabilities. Figure 11 shows the distributions of the composite amplification factors. Transition is located at the intersection point between the curves and the blue line where the composite amplification factor, *N*, is unity. The amplification factor distributions of C-F instability are given in Figure 12. On the upper surface of the baseline, the C-F amplification factor is maintained at a low level, and transition is mainly determined by the development of T-S instability. After optimization, transition location changes little, as shown in Figure 11, but C-F instability becomes dominant at a higher sweep angle. On the lower surface, C-F amplification factor is much larger than the upper surface. Transition location is both determined by C-F instability for the baseline and optimized wing and it moves from x/c=0.137 to x/c=0.073 after optimization. To better understand the mechanism of C-F instability development, Fig.13 compares the crossflow velocity profiles and the results at different streamwise positions upstream of the transition location are shown. The C-F velocity w is scaled by the freestream velocity. As the sweep increases by optimization, the C-F velocity profiles on both surfaces increase. Referring back to Eq.(5), the maximum C-F velocity has a direct effect on the C-F amplification rate. An increased C-F velocity

results in a steeper growth of the amplification factor, as shown in Figure 12. Note that the C-F velocity near the leading edge is relatively large leading to a significant amplification of C-F instability.

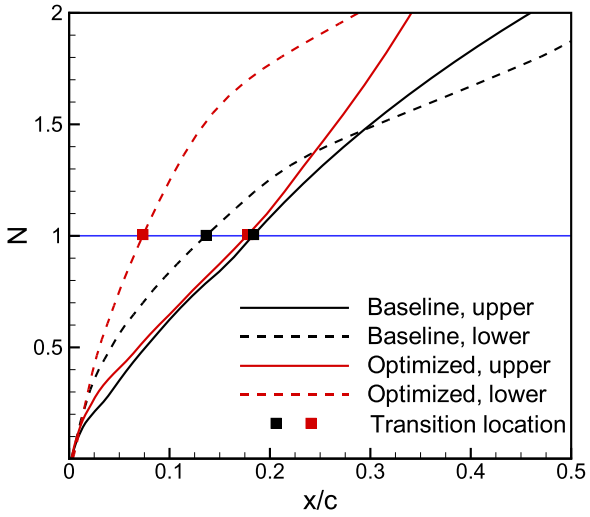

Fig.11 Comparison of the composite amplification factor distributions on the wing's upper and lower surfaces.

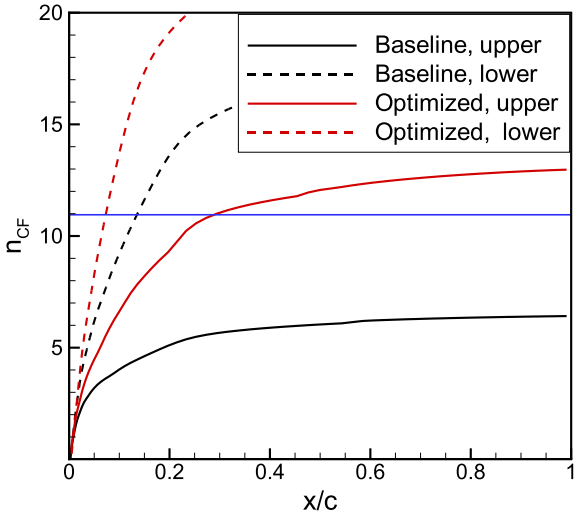

Fig.12 Comparison of the C-F amplification factor distributions on the wing's upper and lower surfaces.

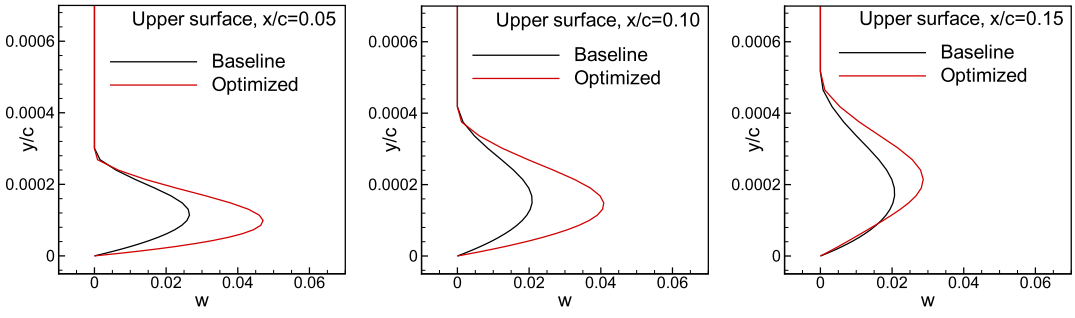

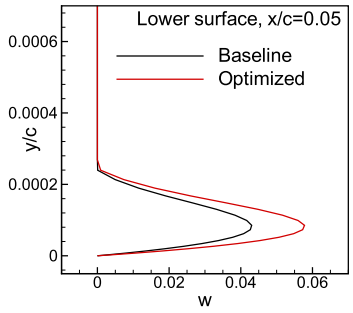

Fig. 13 Comparison of crossflow velocity profiles in the laminar boundary layer at various streamwise locations on the wing.

Table 3 summarizes quantitatively the design objectives, constraints and key design parameters, including force coefficients, transition locations and sweep angle with the lift and attachment-line transition constraints. The A-L transition criterion of both the baseline and optimized wings is far below the critical value, 245. The total drag of the optimized wing decreases by 9.5 drag counts, all from the reduction of pressure drag (including wave drag). The skin friction drag shows 2.4 counts penalty primarily due to the reduction of the laminar area on the lower surface.

Table 3 Optimization results of the baseline and optimized wings.

	C_l	$\bar{R}$	C_d	C_{dp}	C_{df}	$x_{tr,upper}/c$	$x_{tr,lower}/c$	*Sweep angle*
Baseline	0.5	90.4	0.00814	0.00373	0.00441	0.183	0.137	20.0°
Optimized	0.5	109.6	0.00719	0.00254	0.00465	0.176	0.073	28.6°

For this case with a strong shock wave on the baseline upper surface, the total drag reduction for the optimized shape comes from the shock wave alleviation. Compressibility effects have been moderated due to the increased sweep angle and airfoil shaping but C-F instability becomes dominant triggering earlier transition and laminar flow area fails to expand. This highlights the conflicting requirements from laminar flow extension and wave drag reduction for transonic wings.

B. Combined Optimization of an Infinite Swept Wing with 3-D Shock-Control Bump

In order to achieve the extension of the laminar flow while keeping the shock wave under control for the present transonic condition, a combined optimization of an infinite swept wing with a 3-D shock-control bump is investigated. The infinite swept wing is controlled by 18 parameters as in the previous case. The 3-D SCB controlled by 6 parameters is directly added to the upper surface of the wing. As a result, the problem has 24 design variables in total for the wing. The initial geometry is the same as the previous case. After a grid refinement study, 21 nodes equally distributed along the spanwise direction are adopted to resolve the flow around the 3-D bump.

Same as those in the last section, the optimization was conducted at a Mach number of 0.78, a minimum lift coefficient C_l^* of 0.5 and the Reynolds number of 15×10^6. Figure 14 compares the sectional profiles of the baseline and optimized shape in bump crest section at z/c=0.12. The SCB around x/c=0.68 could clearly be seen. The optimized bump parameters are summarized in Table 4.

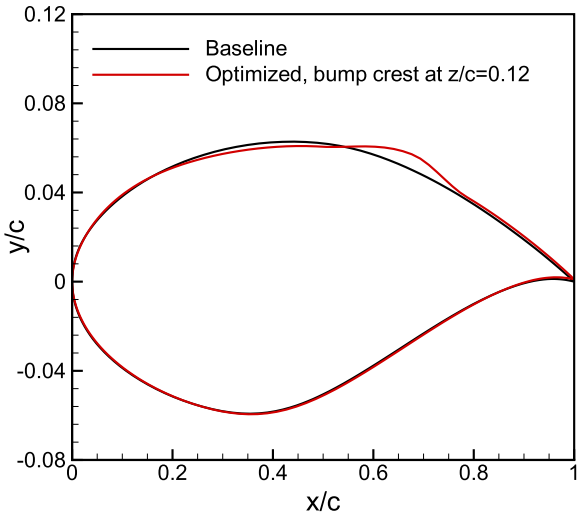

Fig.14 Comparison of the sectional profiles.

Table 4 The optimized 3-D bump parameters.

Length/c	*Crest/c*	*Relative crest*	*Height/c*	*Total span/c*	*Relative Span*
0.29	0.68	0.64	0.0068	0.24	100%

Figures 15 to 17 show the pressure contours of the baseline and the optimized wing with bump at the sections of bump crest (z/c=0.12) and between SCBs (z/c=0) where the periodic boundary condition is applied. The optimized bump replaces the original normal shock wave with more gradual compression waves. Spanwise variations can be observed in the surface pressure contours in Figures 16 and 17 for the wing with SCB. The shock-control effect by the SCB is further demonstrated in the streamwise pressure distributions in Figure 18. The pressure coefficient distributions upstream of the bump are almost identical in different spanwise sections. Contrasting to the case without SCB, the optimization leads to a significant reduction of the sweep angle from 20° to 13.1°, suppressing the crossflow instabilities development as analyzed later.

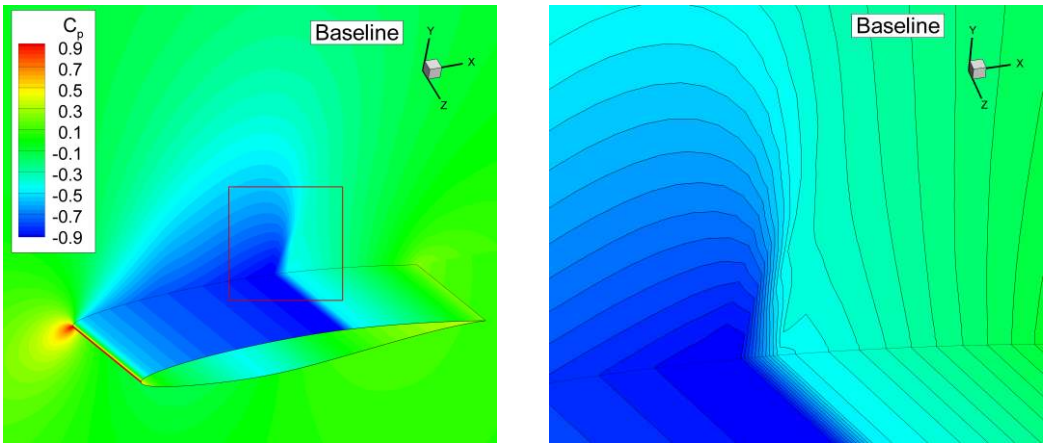

a) Overall trend **b) Around the shock**

Fig.15 Pressure coefficient contours of the baseline wing.

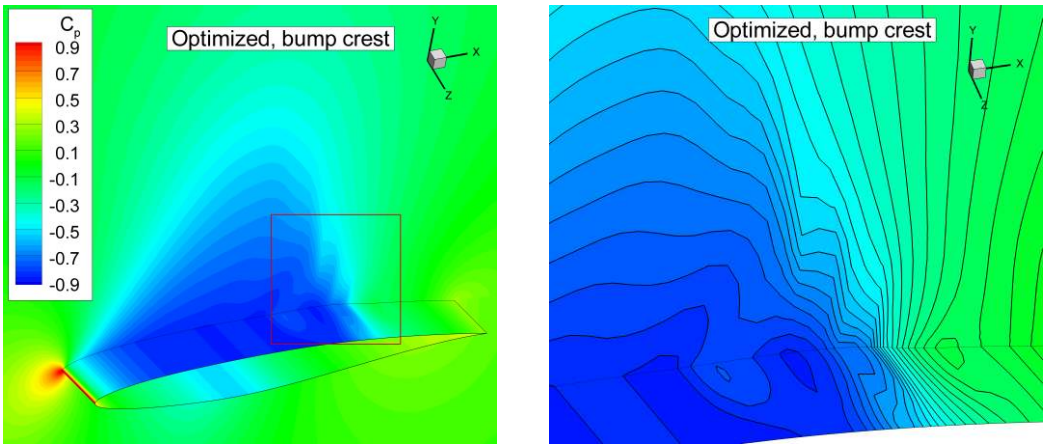

a) Overall trend **b) Around the bump**

Fig.16 Pressure coefficient contours at the bump crest section of the optimized wing with SCB.

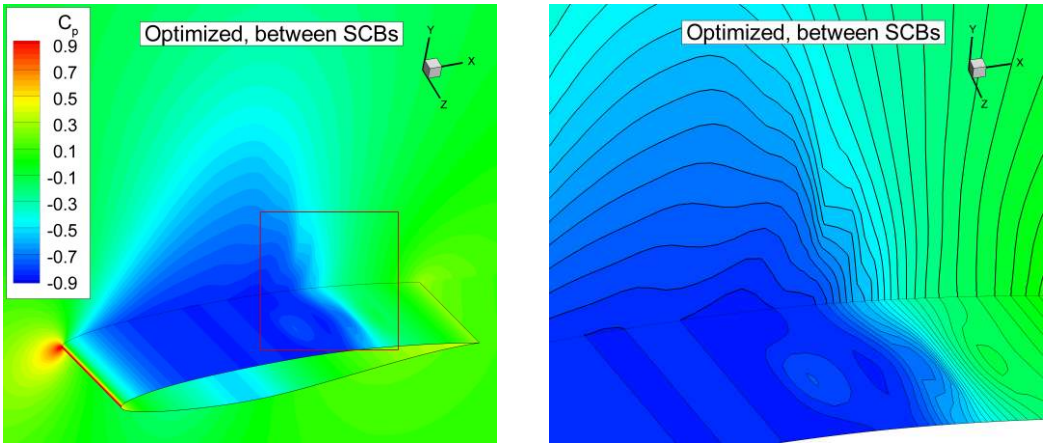

a) Overall trend **b) Around the bump**

Fig.17 Pressure coefficient contours at the section between SCBs of the optimized wing with SCB.

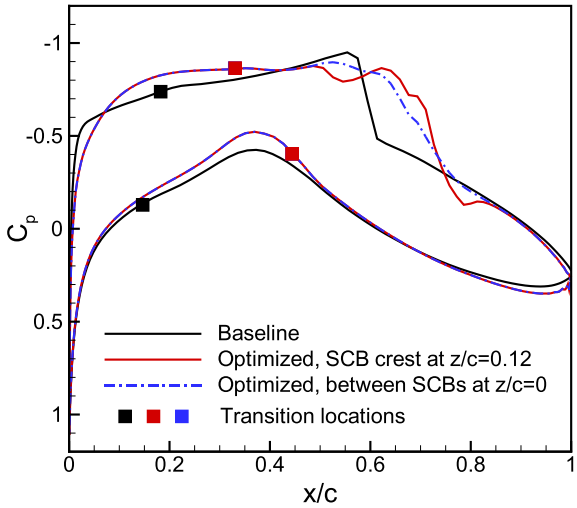

Fig.18 Comparison of the pressure coefficient distributions.

Figures 19 and 20 give the skin friction coefficient contours of the baseline wing and optimized wing with SCB. Transition onsets are shown in the figures followed by a short transition region and fully turbulent flows downstream. The transition onsets on the optimized wing with SCB show a clear delay and the values of skin friction coefficient are lower, especially on the lower surface. The skin friction contour on the upper surface has spanwise variations in the bump region, as shown in Figure 20(a). But the flows upstream the bump region look identical in different spanwise sections.

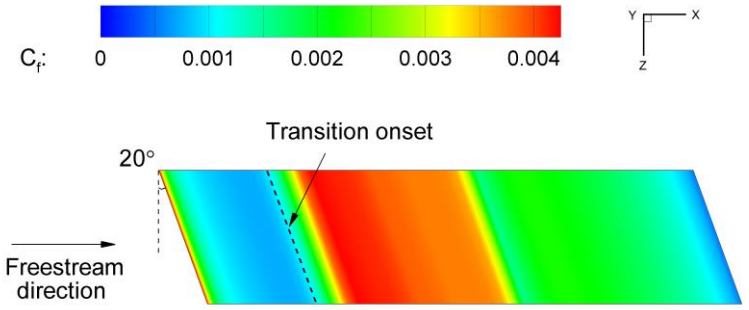

a) Upper surface

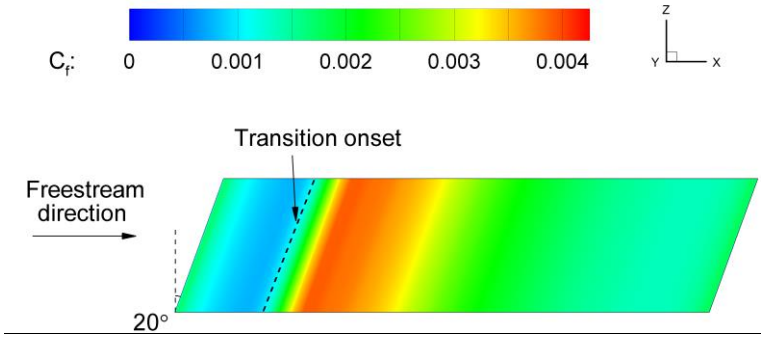

b) Lower surface

Fig.19 Skin friction coefficient contours on the baseline wing.

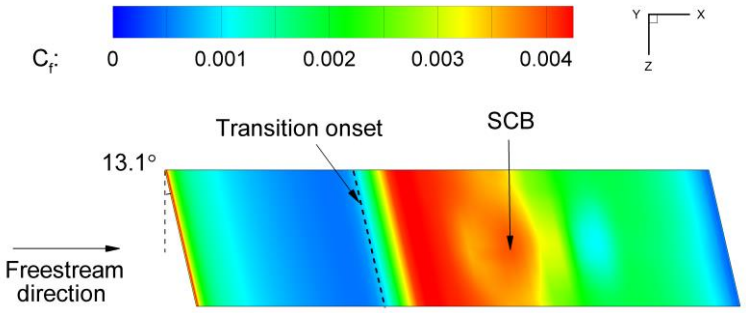

a) Upper surface

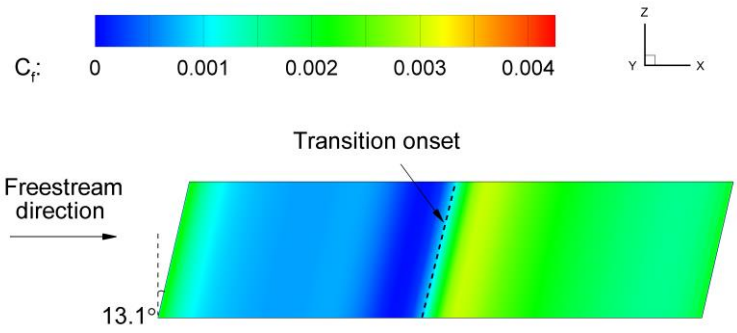

b) Lower surface

Fig.20 Skin friction coefficient contours on the optimized wing with SCB.

Figure 21 compares the skin friction coefficient distributions on each surface of the wings. It can be seen a clearly delayed transition onset on both the upper and lower surfaces after optimization. In the sections of bump crest and between SCBs, the values of skin friction coefficient vary only in the bump region, demonstrating the SCB has very little effect on the upstream flows on the upper surface. Flows around the wings are all fully attached including in the SCB region.

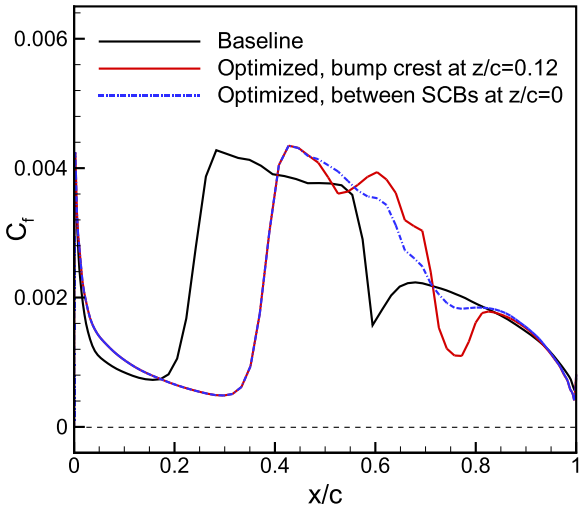

a) Upper surface of the wing

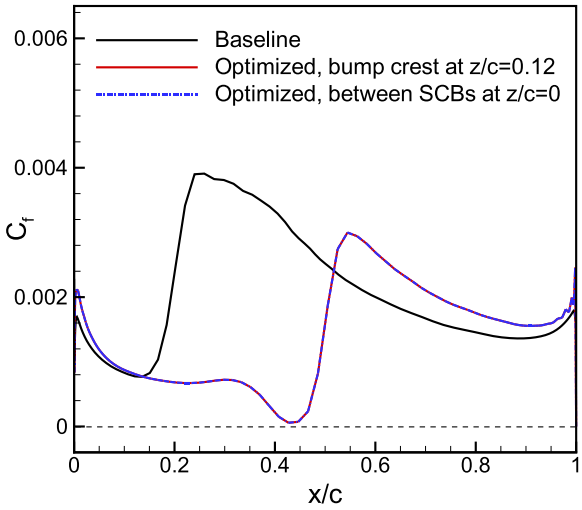

b) Lower surface of the wing

Fig.21 Comparison of the skin friction coefficient distributions.

Figure 22 compares the composite amplification factor distributions for the baseline and optimized wing with SCB. As the results at different spanwise sections are very similar, only the data at bump crest section is given. A notable delay of transition location can be observed for the optimized wing with SCB. Figure 23 shows the C-F amplification factors distributions. It can be seen in Figure 23 that the C-F instability is suppressed after optimization thanks to the lower sweep angle. This effect is more significant on the lower surface. The C-F velocity profiles at different streamwise positions on the lower surface are compared in Figure 24. It can be seen that as a lower sweep angle of 13.1° is obtained after optimization, the C-F velocity decreases, suppressing the development of C-F instability and delaying transition.

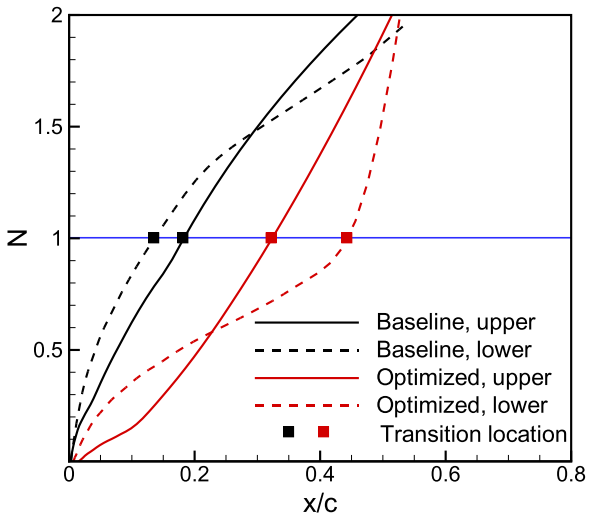

Fig.22 Comparison of the composite amplification factor distributions on the wing's upper and lower surfaces.

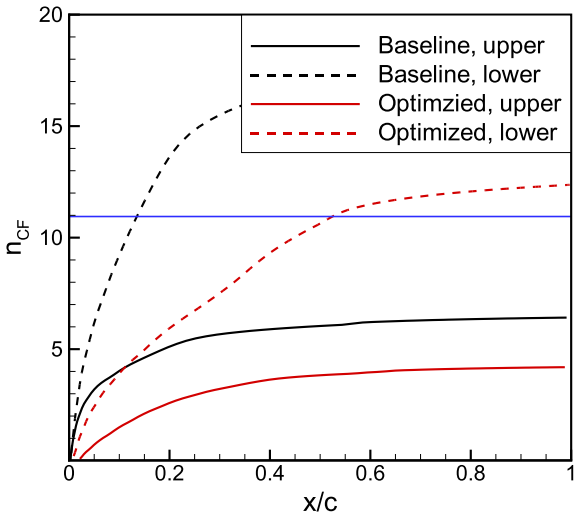

Fig.23 Comparison of the C-F amplification factors distributions on the wing's upper and lower surfaces.

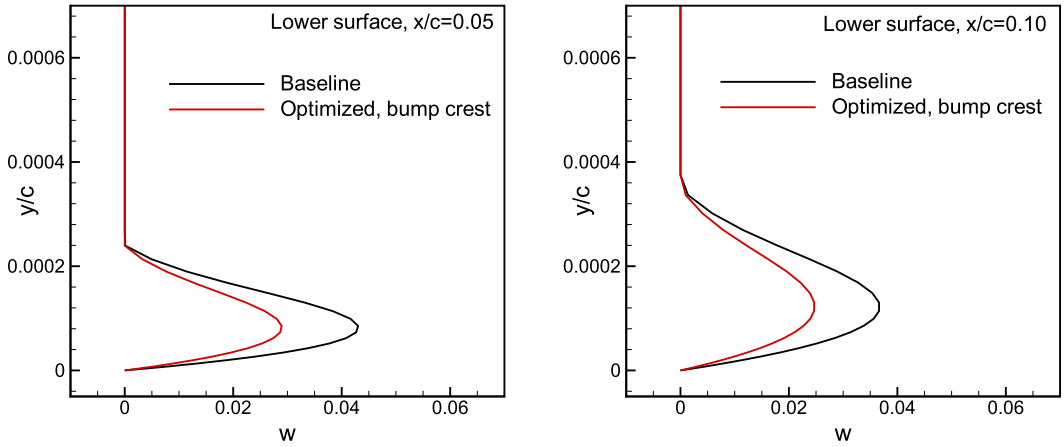

Fig.24 Comparison of crossflow velocity profiles on the lower surface of the wing.

Table 5 summarizes the optimization results. The total drag decreases by 22.9%, or 18.6 drag counts. This is a significant reduction compared with the baseline and the optimization results of last section thanks to the delayed transition locations, which contributes to 10.0 counts reduction in skin friction drag, and the effective control of the shock wave by SCB with a pressure drag reduction of 8.6 counts.

Table 5 Optimization results of the baseline wing and optimized wing with SCB

	C_l	$\bar{R}$	C_d	C_{dp}	C_{df}	$x_{tr,upper}/c$	$x_{tr,lower}/c$	*Sweep angle*
Baseline	0.5	90.4	0.00814	0.00373	0.00441	0.183	0.137	20.0°
Optimized	0.5	49.3	0.00628	0.00287	0.00341	0.324	0.443	13.1°

C. Robustness Analysis

The optimized wing in Section V.B has a low sweep angle and a 3-D bump on the upper surface. The robustness of the optimized shape due to changes in the flight condition, such as Mach number and lift coefficient is investigated in this section.

Figure 25 compares the drag variations for the baseline and the optimized shape obtained in Section V.B at a range of Mach numbers with a fixed lift coefficient of 0.5. It can be seen that the optimized wing with SCB achieves drag reduction when the Mach number is below 0.793. As the optimized shape has a lower sweep angle which increases the effective Mach number perpendicular to the leading edge, there is a drag penalty at higher Mach numbers.

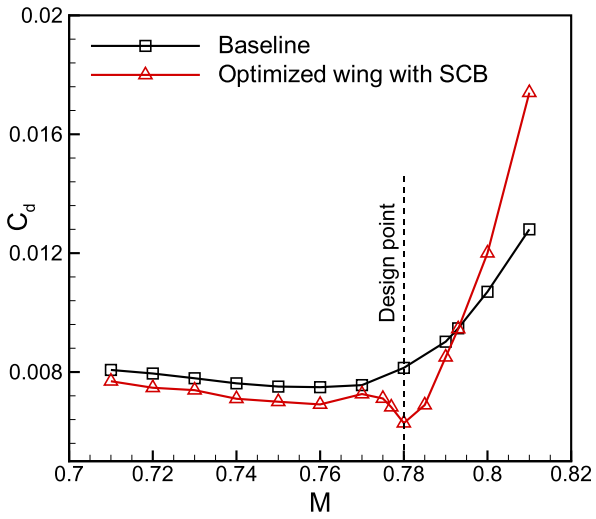

Fig.25 Drag variations at different Mach numbers

Figure 26 shows the robustness for varying lift coefficients between 0.2 and 0.8 at the design Mach number, 0.78. For lower C_l (<0.45), the optimized wing with SCB shows a small drag penalty when compared with the baseline. For C_l between 0.45 and 0.69, the optimized shape shows a reduction in total drag. The drag penalty of the optimized shape increases for C_l higher than 0.69.

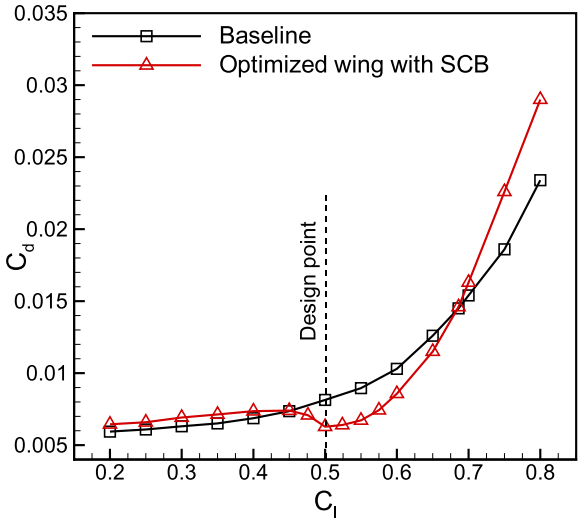

Fig.26 Drag variations at different lift coefficients

To summarize, at the design lift coefficient of 0.5, decreasing the Mach number from 0.793 to 0.71 will maintain the drag reduction. At the design Mach number of 0.78, increasing or decreasing the lift coefficient around the design point will also maintain the drag reduction within a range.

VI. Conclusions

This paper demonstrates that a proper balance of wing sweep and shock-control is crucial for natural laminar flow wing design at a high transonic Mach number of practical importance. Direct introduction of SCB in the optimization process can alleviate the shock wave due to reduced sweep, which in turn allows for better NLF profiling to achieve a larger area of laminar flow. To facilitate this study, a free-transition Reynolds-Averaged Navier-Stokes flow solver and the corresponding discrete adjoint solver incorporating transition criteria have been developed. Both streamwise and crossflow instabilities are integrated.

Aerodynamic shape optimization for an infinite swept wing was conducted at a realistic flow condition for regional transport aircraft at M=0.78. Attachment-line transition is also considered as a constraint to avoid its triggering transition at the leading edge. The wing shape is controlled by 18 parameters for the sectional profile, the incidence and the sweep angle. At this condition of relatively high transonic Mach number, shock wave is a dominant feature on the upper surface so the pressure drag is the main concern. The optimization is successful in alleviating the shock wave to reduce the pressure drag but fails to expand the laminar flow area due to the increase of sweep angle from 20.0° to 28.6°, promoting crossflow instability.

The combined optimization of the wing profile with added 3-D bump leads to a balanced optimization with significant enlargement of the laminar flow region while keeping the pressure drag under control with the SCB. The large laminar flow region is enabled by the reduction of sweep angle from 20.0° to 13.1°, suppressing crossflow instability. The optimized SCB effectively alleviates the shock due to a lower sweep and favorable pressure gradient for NLF profile. Although the flow in the bump region has shown some visible spanwise variations, the effect on the flow upstream of the SCB is negligible.

Acknowledgements

This research is supported by the National Natural Science Foundation (numbers 11432007 and 11672132) and the Priority Academic Program Development of Jiangsu Higher Education Institutions. The first author would also like to acknowledge the Chinese Scholarship Council (number 201706830021) for supporting his research stay at the University of Sheffield.

Reference

1. Kallas, S., Geoghegan-Quinn, M., Darecki, M., Edelstenne, C., Enders, T., Fernandez, E., and Hartman, P., "Flightpath 2050 Europe's Vision for Aviation," European Commission, TR 98, Brussels, Belgium, 2011.
2. Crouch, J. D., "Boundary-Layer Transition Prediction for Laminar Flow Control (Invited)," *45th AIAA Fluid Dynamics Conference*, AIAA Paper 2015-2472, 2015.
   doi:10.2514/6.2015-2472
3. Fujino, M., "Design and Development of the Honda Jet," *Journal of Aircraft*, Vol. 42, No. 3, 2005, pp. 755–764.
   doi:10.2514/1.12268
4. Khayatzadeh, P., and Nadarajah, S. K., "Aerodynamic Shape Optimization of Natural Laminar Flow (NLF) Airfoils," *50th AIAA Aerospace Sciences Meeting*, AIAA Paper 2012-0061, Jan. 2012.
   doi:10.2514/6.2012-61
5. Driver, J., and Zingg, D. W., "Numerical Aerodynamic Optimization Incorporating Laminar-Turbulent Transition Prediction," *AIAA Journal*, Vol. 45, No. 8, 2007, pp. 1810–1818.

doi:10.2514/1.23569

6. Rashad, R., and Zingg, D. W., "Aerodynamic Shape Optimization for Natural Laminar Flow Using a Discrete-Adjoint Approach," *AIAA Journal*, Vol. 54, No. 11, 2016, pp. 3321–3337.

   doi:10.2514/1.J054940

7. Amoignon, O. G., Pralits, J. O., Hanifi, A., Berggren, M., and Henningson, D. S., "Shape Optimization for Delay of Laminar-Turbulent Transition," *AIAA Journal*, Vol. 44, No. 5, 2006, pp. 1009–1024.

   doi:10.2514/1.12431

8. Zhao, K., Gao, Z., and Huang, J., "Robust Design of Natural Laminar Flow Supercritical Airfoil by Multi-Objective Evolution Method," *Applied Mathematics and Mechanics*, Vol. 35, No. 2, Jan. 2014, pp. 191–202.

   doi:10.1007/s10483-014-1783-6

9. Campbell, R. L., and Lynde, M. N., "Natural Laminar Flow Design for Wings with Moderate Sweep," *34th AIAA Applied Aerodynamics Conference*, AIAA Paper 2016-4326, 2016.

   doi:10.2514/6.2016-4326

10. Schrauf, G., "Stability Analysis of the F100 Flight Experiment—A Second Look," Daimler-Benz Aerospace Airbus, ELFIN II Rept. 173, Bremen, Germany, Jan. 1996.

11. Qin, N., "Drag Reduction for Transonic Wings Combining Reduced Wing Sweep with Shock Control," *28th International Symposium on Shock Waves*, Vol. 1, Springer–Verlag, Berlin, Jan. 2012, pp. 45–53.

    doi:10.1007/978-3-642-25688-2_7

12. Seitz, A., Hübner, A. and Risse, K., "The DLR TuLam Project: Design of a Short and Medium

Range Transport Aircraft with Forward Swept NLF Wing," *CEAS Aeronautical Journal*, Vol. 11, 2020, pp. 449–459.

doi:10.1007/s13272-019-00421-1

13. Zhang, Y. F., Fang, X., Chen, H., Fu, S., Duan, Z., and Zhang, Y., "Supercritical Natural Laminar Flow Airfoil Optimization for Regional Aircraft Wing Design," *Aerospace Science and Technology*, Vol. 43, June 2015, pp. 152–164.

doi:10.1016/j.ast.2015.02.024

14. Han, Z., Chen, J., Zhang, K., Xu, Z., Zhu, Z., and Song, W., "Aerodynamic Shape Optimization of Natural Laminar Flow Wing Using Surrogate-Based Approach," *AIAA Journal*, Vol. 56, No. 7, 2018, pp. 2579–2593.

doi: 10.2514/1.J056661

15. Lee, J., and Jameson, A., "Natural-Laminar-Flow Airfoil and Wing Design by Adjoint Method and Automatic Transition Prediction," *47th AIAA Aerospace Sciences Meeting and Exhibit*, AIAA Paper 2009–0897, Jan. 2009.

doi:10.2514/6.2009-897

16. Williams, G., "Aerospace Technology Demonstration: BLADE, the Flagship Laminar Flow Project Within the Clean Sky Programme," Soc. of Automotive Engineers TP 2017-01-2016, Fort Worth, TX, Sept. 2017.

doi:10.4271/2017-01-2016

17. König, J., and Thomas, H., "The Clean Sky Smart Fixed Wing Aircraft Integrated Technology Demonstrator: Technology Targets and Project Status," *Proceedings of the 27th International Congress of the Aeronautical Science*, Vol. 6, ICAS, Stockholm, Sweden, 2010, pp. 5101–5110.

18. Streit, T., Wedler, S. and Kruse, M., “DLR Natural and Hybrid Transonic Laminar Wing Design Incorporating New Methodologies,” *Aeronautical Journal*, Vol. 119, No. 1221, 2015, pp. 1303–1326.
doi:10.1017/S0001924000011283

19. Fage, A. and Sargent, R.F., “Effect on Aerofoil Drag of Boundary Layer Suction Behind a Shock Wave,” ARC R&M No. 1913, 1943.

20. Ashill, P. R., Fulker, J. L., and Shires, A., “A Novel Technique for Controlling Shock Strength of Laminar-Flow Aerofoil Sections, ” DGLR Bericht 92-01, 1992, pp. 175–183

21. Stanewsky, E., Delery, J., Fulker, J., and de Matteis, P., “Synopsis of the Project EUROSHOCK II,” *Notes on Numerical Fluid Mechanics and Multidisciplinary Design: Drag Reduction by Shock and Boundary Layer Control—Results of the Project EUROSHOCK II*, Vol. 80, Springer-Verlag, Berlin, 2002, pp. 1–124.

22. König, B., Pätzold, M., Lutz, T., and Krämer, E., “Numerical and Experimental Validation of Three-Dimensional Shock Control Bumps,” *Journal of Aircraft,* Vol. 46, No. 2, 2009, pp. 675–682.
doi:10.2514/1.41441

23. Birkemeyer, J., Rosemann, H., and Stanewsky, E., “Shock Control on a Swept Wing,” *Aerospace Science and Technology*, Vol. 4, No. 3, 2000, pp. 147–156.
doi:10.1016/S1270-9638(00)00128-0

24. Qin, N., Monet, D., and Shaw, S. T., “3D Bumps for Transonic Wing Shock Control and Drag Reduction,” *CEAS Aerospace Aerodynamics Research Conference*, Royal Aeronautical Soc., Cambridge, England, U.K., 2002, pp. 1–11.

25. Qin, N., Wong, W. S., and Le Moigne, A., "Three-Dimensional Contour Bumps for Transonic Wing Drag Reduction," *Proceedings of the Institution of Mechanical Engineers, Part G: Journal of Aerospace Engineering*, Vol. 222, No. 5, 2008, pp. 619–629.
doi:10.1243/09544100JAERO333

26. Zhu, M., Li, Y., Qin, N., Huang, Y., Deng, F., Wang, Y. and Zhao, N., "Shock Control of a Low-Sweep Transonic Laminar Flow Wing," *AIAA Journal*, Vol.57, No. 6, 2019, pp. 2408–2420.
doi: 10.2514/1.J058011

27. Colliss, S. P., Babinsky, H., Nübler, K., and Lutz, T., "Vortical Structures on Three-Dimensional Shock Control Bumps," *AIAA Journal*, Vol. 54, No. 8, 2016, pp. 2338-2350.
doi:10.2514/1.J054669

28. Tang, Z., Chen, Y. and Zhang, L., "Natural laminar flow shape optimization in transonic regime with competitive Nash game strategy," *Applied Mathematical Modelling*, Vol. 48, 2017, pp. 534–547.
doi:10.1016/j.apm.2017.04.012

29. Bruce, P. J. K., and Colliss, S. P., "Review of Research into Shock Control Bumps," *Shock Waves*, Vol. 25, No.5, 2015, pp. 451-471.
doi:10.1007/s00193-014-0533-4

30. Drela, M. and Giles, M.B., "Viscous-Inviscid Analysis of Transonic and Low Reynolds Number Airfoils," *AIAA Journal*; Vol.25, No. 10, 1987, pp. 1347–1355.
doi:10.2514/3.9789

31. Sturdza, P., "An Aerodynamic Design Method for Supersonic Natural Laminar Flow Aircraft," Ph.D. Dissertation, Dept. of Aeronautics and Astronautics, Stanford Univ., Stanford, CA, 2004.

32. Dagenhart, J. R., “Amplified Crossflow Disturbances in the Laminar Boundary Layer on Swept Wings with Suction,” NASA TP 1902, 1981.

33. Poll, D. I. A., “Transition in the Infinite Swept Attachment Line Boundary Layer,” *Aeronautical Quarterly*, Vol. 30, No. 4, 1979, pp. 607–629.
doi:10.1017/S0001925900008763

34. Le Moigne, A., and Qin, N., “Variable-Fidelity Aerodynamic Optimization for Turbulent Flows Using a Discrete Adjoint Formulation,” *AIAA Journal*, Vol. 42, No. 7, 2004, pp. 1281–1292.
doi:10.2514/1.2109

35. Le Moigne, A., “A discrete Navier-Stokes adjoint method for aerodynamic optimisation of Blended Wing-Body configurations,” Ph.D. Dissertation, Cranfield Univ., Cranfield, England, U.K., 2002.

36. Baldwin, B. S., and Lomax, H., “Thin Layer Approximation and Algebraic Model for Separated Turbulent Flows,” *16th AIAA Sciences Meeting*, AIAA Paper 78-257, Jan. 1978.
doi:10.2514/6.1978-257

37. Mayda, E., “Boundary Layer Transition Prediction for Reynolds–Averaged Navier–Stokes Methods,” Ph.D. Dissertation, Univ. of California, Davis, CA, 2007.

38. Krumbein, A., “Automatic Transition Prediction and Application to 3D Wing Configurations,” *44th AIAA Aerospace Sciences Meeting and Exhibit*, AIAA Paper 2006-914, Jan. 2006.
doi:10.2514/6.2006-914

39. Nebel, C., Radespiel, R., and Wolf, T., “Transition Prediction for 3-D Flows Using a Reynolds-Averaged Navier-Stokes Code and N-Factor Methods,” *33rd AIAA Fluid Dynamics Conference and Exhibit*, AIAA Paper 2003-3593, June 2003.

doi:10.2514/6.2003-3593

40. Le Moigne, A., and Qin, N., "Airfoil Profile and Sweep Optimization for a Blended Wing-Body Aircraft Using a Discrete Adjoint Method," *Aeronautical Journal*, Vol. 110, No. 1111, 2006, pp. 589–604.

    doi:10.1017/S0001924000001457

41. Somers, D. M., "Design and Experimental Results for a Natural-Laminar-Flow Airfoil for General Aviation Applications," NASA TP 1861, June 1981.

42. Boltz, F. W., Kenyon, G. C., and Allen, C. Q., "Effects of Sweep Angle on the Boundary-Layer Stability Characteristics of an Untapered Wing at Low Speeds," NASA TN-D-338, 1960.

43. Shi, Y., Yang, T., Bai, J., Lu, L. and Wang, H., "Research of Transition Criterion for Semi-Empirical Prediction Method at Specified Transonic Regime," *Aerospace Science and Technology*, Vol.88, 2019, pp.95-109.

    doi:10.1016/j.ast.2019.03.012

44. Jackson, P., *Jane's All the World's Aircraft*, Jane's Information Group, London, 2004.